Hindawi
Advances in Materials Science and Engineering
Volume 2023, Article ID 9874265, 1 page
https://doi.org/10.1155/2023/9874265

*Retraction*

# Retracted: Seismic Performance and Finite Element Analysis of Reinforced Concrete Frames Considering a Masonry-Infilled Wall

**Advances in Materials Science and Engineering**

Received 26 December 2023; Accepted 26 December 2023; Published 29 December 2023



This article has been retracted by Hindawi, as publisher, following an investigation undertaken by the publisher [1]. This investigation has uncovered evidence of systematic manipulation of the publication and peer-review process. We cannot, therefore, vouch for the reliability or integrity of this article.

Please note that this notice is intended solely to alert readers that the peer-review process of this article has been compromised.

Wiley and Hindawi regret that the usual quality checks did not identify these issues before publication and have since put additional measures in place to safeguard research integrity.

We wish to credit our Research Integrity and Research Publishing teams and anonymous and named external researchers and research integrity experts for contributing to this investigation.

The corresponding author, as the representative of all authors, has been given the opportunity to register their agreement or disagreement to this retraction. We have kept a record of any response received.

## References

[1] K. Xi and B. Liu, "Seismic Performance and Finite Element Analysis of Reinforced Concrete Frames Considering a Masonry-Infilled Wall," *Advances in Materials Science and Engineering*, vol. 2022, Article ID 6832624, 16 pages, 2022.

Hindawi
Advances in Materials Science and Engineering
Volume 2022, Article ID 6832624, 16 pages
https://doi.org/10.1155/2022/6832624



*Research Article*

# Seismic Performance and Finite Element Analysis of Reinforced Concrete Frames Considering a Masonry-Infilled Wall

**Kailin Xi and Boquan Liu**

*School of Civil Engineering, Chang'an University, Xi'an 710061, China*

Correspondence should be addressed to Kailin Xi; xikailin@sfmail.sf-express.com

Received 28 July 2022; Revised 4 September 2022; Accepted 9 September 2022; Published 10 October 2022

Academic Editor: Haichang Zhang



This study investigated the seismic performance of a 1/3 scale, three-story, and three-span RC frame subjected to static cyclic lateral loading. The failure process and mode were analyzed using the digital image correlation (DIC) method. Based on the test, finite element (FE) models were developed and verified. Using the proposed FE models, the parametric study was performed to investigate the influence of the opening rate, the position of infill walls, and the block strength on the seismic performance of the frame. Test results indicated that FE simulation results are correspondent to the testing results. The infilled wall increased the horizontal bearing capacity of the structure and the energy dissipation capacity. The opening masonry-infilled wall reduced the energy consumption capacity and the initial stiffness of the structure. Removing the infill walls on the first floor would change the failure mode of the frame. Improving the block strength could improve the bearing capacity of frames but has little effect on the energy dissipation capacity of the frame.

## 1. Introduction

Infilled masonry walls (IMW) are widely utilized as cladding or partitions in reinforced concrete (RC) and steel moment-resisting frames. Although it is commonly accepted that the mutual influences between the infill wall and RC frame affect the overall structural behavior, as well as the failure mechanism of the frame, they are often ignored in design practice [1–3]. Due to the need for lighting and the use function, openings are commonly found on the infill walls [4]. Furthermore, the existence of openings made the damage to the infill wall more complicated [5]. Openings altered the force transferring of the infill wall and significantly affected the infilled frame's seismic performance [6]. Studying the seismic performance of infilled RC frame with opening and finding a reasonable analytical model to assess the influence of the opening infill wall on the frame structure become an important research topic.

In order to investigate the seismic behavior of RC frames with IMW, plenty of experimental tests have been conducted. Moreover, they indicated that the masonry-filled wall can significantly improve the seismic performance and strength of the frame structure [7–11]. Wang et al [12] investigated the seismic behavior of masonry-infilled reinforced concrete (RC) frames under horizontal loading. It was found that the performance of RC frames was significantly improved with or without holes in the infilled wall. Penava et al [13] explored the influence of the opening type, size, and position on the shear resistance and deformation capacity of single components in the masonry-infilled RC frame structure. The test results indicated that the type of opening has a certain influence on the design characteristics of the infilled RC frame. Zovkic [14] investigated various kinds of masonry infills to the behavior of RC frames under horizontal loads. The results showed that the composite "framed wall" structure had much higher stiffness, damping, and initial strength than the bare frame structure. Furthermore, many scholars have studied the failure modes of infilled walls to investigate the influence of infilled walls on RC frame structures under horizontal load. Zhang et al [15] completed the low-cycle reciprocating loading test of the recycled masonry-filled wall-steel recycled concrete frame structure, and the

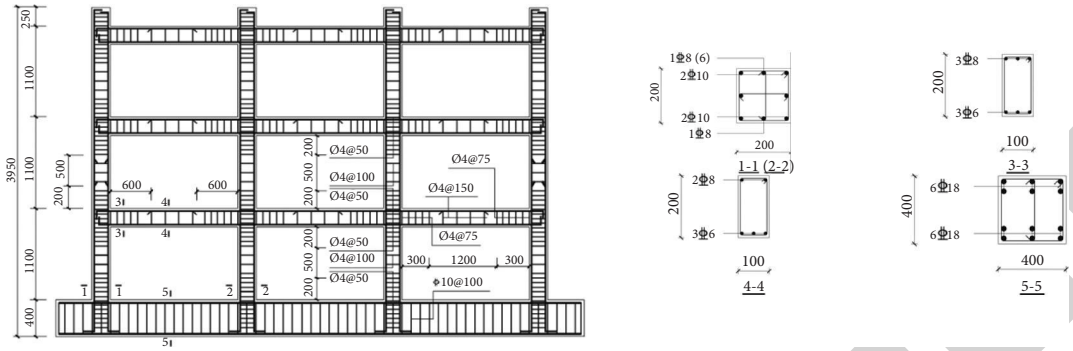


Figure 1: The size of the specimens.

research showed that the failure mode of bare frame and frame with the filled wall was a ductile failure. Basha and Kaushik [16] studied the seismic performance of the single-layer frame masonry infill wall and found that even though the strength of the infill wall was very weak, the column still mainly suffered a shear failure.

To further evaluate the influence of various influencing factors on the seismic performance of infilled wall RC frame structure, many scholars have proposed and verified some finite element simulation methods of masonry-infilled wall on the RC frame structure [17, 18]. Jin et al [19] based on the quasistatic test of the filled wall frame and the DIANA nonlinear finite element analysis program, and a separated microscopic finite element model of the filled wall frame structure was established. Mohammad et al [20] completed the finite element nonlinear static analysis of the masonry-filled wall frame structure and gave the damage mode and capacity curve of the specimen. The results show that the numerical simulation can respond well to the test results. Dolatshahi [21] adopts numerical simulation to evaluate the seismic performance of the unreinforced masonry wall, and the results show that the in-plane loading pattern is more important in walls with higher aspect ratios. Mallick and Severn [22] and Mallick and Garg [23] suggested using interface elements to simulate the slip between the frame and the wall. The model established by Liauw et al [24] considered the isotropy of the infilled wall before cracking and the anisotropy after breaking. A simple rod element was used to simulate the wall frame interface to assess the separation and slip of the interface. Asteris [25, 26] proposed a step-by-step analysis method to determine the contact length and interface stress. This method assumes that the infilled wall and the frame cannot overlap. Lotfi and Shing [27] established a homogenized finite element model of masonry to simulate the bending response of masonry walls. In the first mock exam, Koutromanos et al [28, 29] improved this model to affect the mechanical performance of masonry walls under dynamic loads. Lourenco and Rots [30] put forward the calculation method of normal and tangential stiffness of interface elements between blocks and analyzed the mechanical properties of masonry walls under monotonic load by using a simplified micromodel.

This paper studied the seismic performance of RC frames through pseudostatic testing, and the influence of different openings, locations, and block strengths of masonry-infilled walls on seismic performance was analyzed by the finite element technique. The influence of different parameters on the seismic behaviors of retrofitted frames was evaluated in terms of hysteretic curves, skeleton curves, energy dissipation, stiffness degradation, ductility, and failure characteristic, which can provide a reference and theoretical basis for the design.

## 2. Experimental Program

*2.1. Specimens.* In this study, a 1/3 scaled, three-story, and three-span reinforced concrete frame was cast. Figure 1 shows the dimensions and reinforcing details of the specimens. The height of the frame is 3950 mm and the span of the frame is 2000 mm. The height/length ratio is about1.98:1 . The beam and column cross section were 100 mm (width) ×200 mm (depth) and 200 mm (width) ×200 mm (depth). Tables 1 and 2 show the measured properties of concrete and reinforcements, respectively.

*2.2. Test Setup Instrumentation.* Figure 2 shows the experimental setup of a typical specimen. The specimen was fixed to the strong floor by foundation beams and set to the firm base by anchorage. The low cyclic lateral load was applied by a 100 *t* MTS electrohydraulic servo actuator securely fixed to the reaction wall. The floor load of the frame structure is converted into the top vertical load in this test, which is synchronously applied by hydraulic jacks at the top of each column. The hydraulic Jack was manually adjusted at the end of each load step to ensure the axial force in the queue was almost constant during tests until the vertical bearing capacity decreased significantly.

Figure 3 shows that a displacement-control loading procedure was applied in this study. The low-cycle cyclic load is used on the centerline of the top frame beam. In the initial increments, the loading displacement step of each stage is 3 mm, and each stage is loaded once. After the frame yields, the loading displacement at all levels increases by 9 mm, and each level is loaded for three cycles until the loading displacement is 135 mm; that is, the frame structure is considered to have collapsed.

The digital image correlation method is used to record the crack development and related data to reduce the observation error. Five high-resolution cameras are used to

Table 1: Concrete properties in different parts.

| Parts | $f_c$ (MPa) | $f_{ck}$ (MPa) | $f_{tk}$ (MPa) | $E_c$ (MPa) |
|---|---|---|---|---|
| First floor | 30.48 | 23.16 | 2.58 | 29942.24 |
| Second floor | 21.82 | 16.58 | 2.15 | 26370.49 |
| Top floor | 33.18 | 25.21 | 2.71 | 30797.50 |

$F_c$ is cylindrical compressive strength; $f_{ck}$ is uniaxial compressive strength; $f_{tk}$ is uniaxial tensile strength; $E_c$ is elastic modulus.

Table 2: Properties of reinforcements.

| Types | $d$ (mm) | Yield strength (MPa) | Ultimate strength (MPa) |
|---|---|---|---|
| Low carbon steel wire | 4 | 2014 | 678.6 |
| HRB400 | 6 | 471.2 | 606.2 |
| HRB400 | 8 | 548.9 | 640.2 |
| HRB400 | 10 | 539.2 | 593.7 |

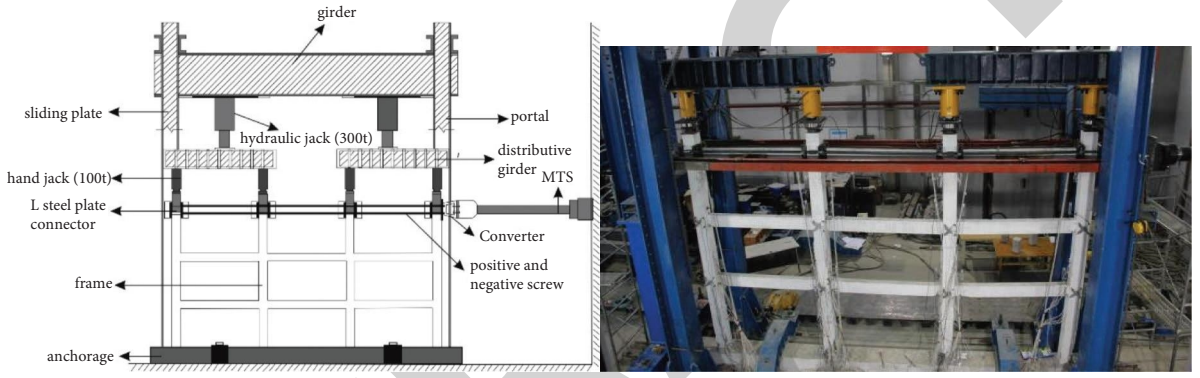


Figure 2: Schematic diagram of the test loading device.

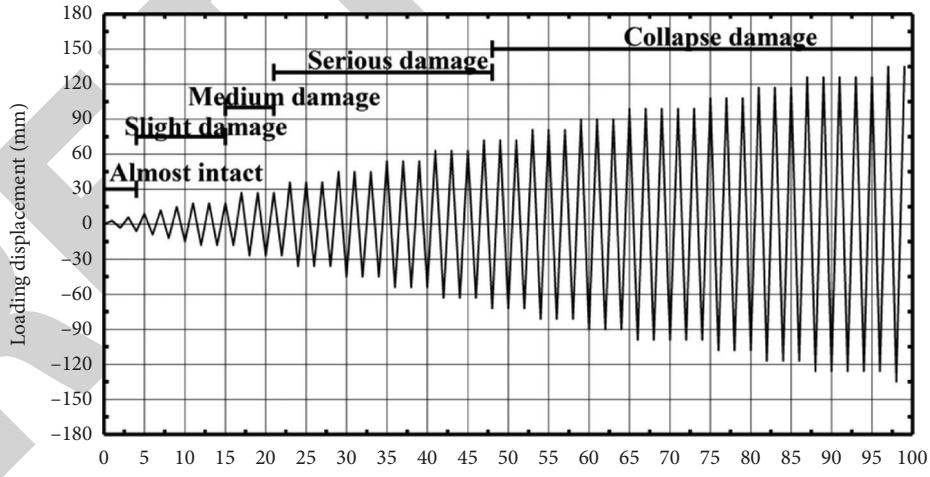


Figure 3: Applied lateral displacement history.

capture the deformation images of the structure at each stage to ensure the accuracy of the measured data. A camera whose resolution is $5472 \times 3648$ is used to capture the overall deformation of the frame. Four cameras, whose resolution is $5184 \times 3456$, are used to capture the local member deformation. Ncorr-V1.2 analyses the collected digital images, and the data, such as the local deformation program of a beam, column, and overall structure, are obtained.

## 3. Experimental Results and Discussion

*3.1. Experimental Behavior.* Some slightly visible bending cracks emerged at the beams' ends and midspan when the displacement was 3 mm. Then, the cracks continued to elongate gradually, and the number and range of gaps increased obviously with the increasing displacement amplitude. In the loops of 63 mm displacement, the concrete at the bottom of the

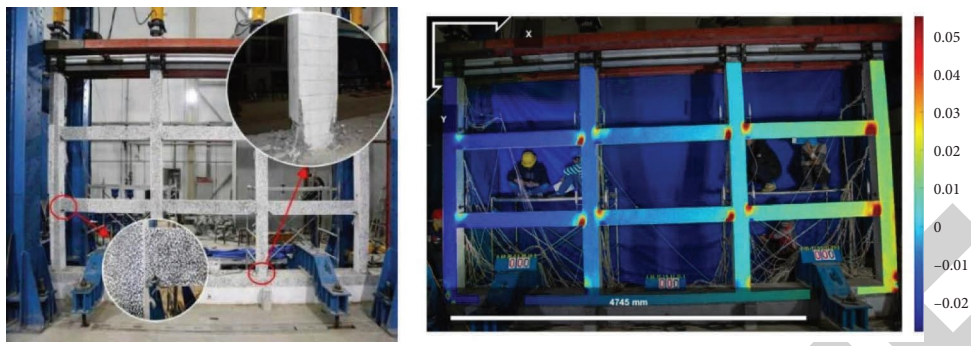


Figure 4: The failure mode.

beams' ends began to fall off, and cracks appeared at the joints. The concrete at the foot of the side columns started to crack and peel. Finally, some tensile reinforcements in the bottom of the beams were exposed and buckled when the displacement reached 135 mm, and the test was ended. All nodes were approximately intact, on which no X-type cracks arose.

*3.2. Failure Mode.* Figure 4 shows the failure mode of the test frame. The concrete at the columns foot was crushed, and the steel bars in the middle columns yielded to plastic hinges. The concrete at all the beams' ends fell off, and the steel bars in the – first floor beams ruptured or yielded, while the steel bars in the second floor beams only yielded. At this time, the frame was deemed in the collapse stage, and the interstory displacement angle had been nearly 1/24, which far exceeded the limit of 1/50 and 1/40 for the elastoplastic interstory displacement angle limits of reinforced concrete frame structures in GB 50011–2010 [31] and ASCE 7–10 [32], respectively.

*3.3. Hysteretic and Skeleton Curves.* The hysteretic and skeleton curves of the test specimen are shown in Figure 5: The hysteretic and skeleton curves are crucial in investigating the nonlinear seismic response. They reflect the strength, energy dissipation, and deformation characteristics of a specimen. Figure 5 shows that before the specimen yielded, the bearing capacity increased linearly with the displacement, the residual deformation was small, and the stiffness degradation was not apparent. Then, with the increasing displacement, cracks appeared and continued to increase and reinforcements began to yield. The specimen exhibited elastoplasticity. The hysteretic curve of the specimen exhibited an "arc" shape after yielding. When the displacement increased to +19.05 mm and −18.87 mm, the bearing the capacity of specimen reached the maximum which was 154.1 kN and −143.0 kN, respectively. Then, the bearing capacity began to decrease. The test was stopped when the load declined to 85% of the peak load.

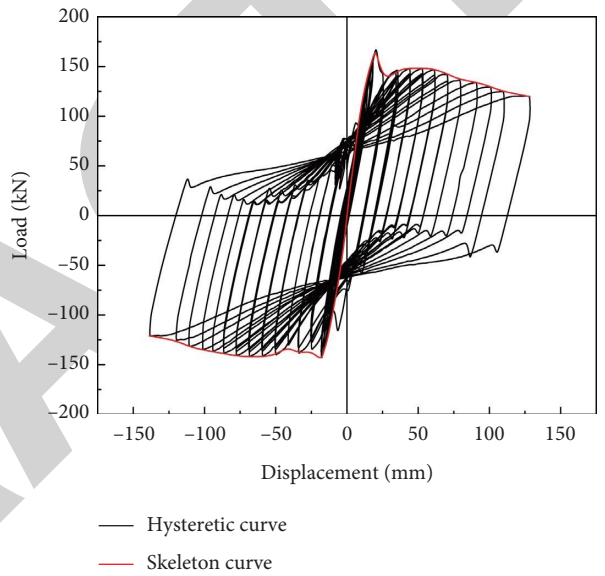


Figure 5: The hysteretic and skeleton curves of the test specimen.

## 4. Finite Element Analysis

*4.1. Finite Element Modelling.* Previous studies [12–14] have shown that the seismic behavior of frames would be underestimated without considering the effect of the infilled walls. However, up to now, the effect of the infill wall on the seismic behavior of frames has not been considered in seismic codes due to inadequate studies. Therefore, in this section, the effect of infill walls on the seismic behavior of frames will be further studied with ABAQUS software based on the experimental results. The variables include openings, the position of infill walls, and the strength of blocks. The detailed descriptions of specimens are shown in Table 3. The C3D8R elements were used to create the concrete frame and masonry infilled walls, while the reinforcement was modeled by 2-node truss elements (T3D2). The walls were established through the monolithic model and rigidly connected to the frame. Further, the steel bars cage was embedded into the whole model to realize the deformation coordination between the reinforcement and concrete, and the bottom beam was fully constrained.

*4.2. Material Modelling.* To explicitly record the overall behavior of the frames, the mechanical property of concrete was simulated by the concrete damaged plastic (CDP) model and that of the steel bars was used by the elastoplastic model with progressive damage.

*4.3. CDP Model.* The CDP model [33–35] assumes the evolution of the yield surface depends on the strength function of the effective stress, and the effect of damage on

Table 3: Infilled wall layout.

| Specimen | Strength grades of blocks | Filling walls and the ratio of holes |
|---|---|---|
| KJ-1 | Same as a test specimen | No walls |
| KJ-T-1 | MU10 + Mb5 | Openings rate 0% |
| KJ-T-2 | MU10 + Mb5 | Opening rate 10% |
| KJ-T-3 | MU10 + Mb5 | Opening rate 20% |
| KJ-T-4 | MU10 + Mb5 | Opening rate 30% |
| KJ-T-5 | MU10 + Mb5 | The filling walls were distributed on the second and third floor with an openings rate of 0% |
| KJ-T-6 | MU10 + Mb5 | The filling walls were distributed on the second and third floor with an openings rate of 30% |
| KJ-T-7 | MU20 + Mb5 | Opening rate 30% |
| KJ-T-8 | MU30 + Mb5 | Opening rate 30% |

Note: MU represents the strength grade of concrete block; Mb is the strength grade of mortar.

the loading and unloading stiffness during the crack opening and closing process is considered. Figure 6 shows the yield surfaces and deviatoric plane of the model. The yield function is as follows:

$$F = \frac{1}{1-\alpha}\left[\overline{q} - 3\alpha\overline{p} + \beta\left(\widetilde{\varepsilon}_t^{pl}, \widetilde{\varepsilon}_c^{pl}\right)\langle\widehat{\sigma}_{\max}\rangle - \gamma\langle -\widehat{\sigma}_{\max}\rangle\right] - \overline{\sigma}_c\left(\widetilde{\varepsilon}_c^{pl}\right),$$

$$\overline{p} = -\frac{1}{3}\operatorname{tr}(\sigma),$$

$$\overline{q} = \sqrt{\frac{3}{2}\|\operatorname{dev}(\sigma)\|},$$

$$\alpha = \frac{(\sigma_{b0}/\sigma_{c0}) - 1}{2(\sigma_{b0}/\sigma_{c0}) - 1}; 0 \le \alpha \le 0.5,$$

$$\beta = \frac{\overline{\sigma}_c\left(\widetilde{\varepsilon}_c^{pl}\right)}{\overline{\sigma}_t\left(\widetilde{\varepsilon}_t^{pl}\right)}(1-\alpha) - (1+\alpha),$$

$$\gamma = \frac{3(1-K_c)}{2K_c - 1}, \tag{1}$$

where $p$ is the hydrostatic stress; $q$ is the Mises equivalent stress; $\widetilde{\varepsilon}_t^{pl}$ is the plastic tension strain; $\widetilde{\varepsilon}_c^{pl}$ is the plastic compression strain; $\widehat{\sigma}_{\max}$ denotes the maximum principal stress; $\sigma$ represents the stress tensors; $\sigma_{b0}/\sigma_{c0}$ is the ratio of initial equal biaxial compression yield stress to initial uniaxial compression yield stress; $\overline{\sigma}_t(\widetilde{\varepsilon}_t^{pl})$ and $\overline{\sigma}_c(\widetilde{\varepsilon}_c^{pl})$ are the tension and compression cohesion, assumed to depend on $\widetilde{\varepsilon}_t^{pl}$ and $\widetilde{\varepsilon}_c^{pl}$, respectively; $K_c$ indicates the ratio of the second stress invariant on the tensile meridian to that on the compressive meridian, which was taken as 2/3 according to the study of Lubliner et al [34].

*4.4. Concrete Constitutive Models.* The concrete compressive and tensile stress-strain relationships proposed by GB 50010–2010 [36]were adopted in this study, which are expressed as follows:

*4.4.1. Compressive Behavior*

$$y = \begin{cases} a_a x + (3 - 2a_a)x^2 + (a_a - 2)x^3, & x \le 1, \\ \dfrac{x}{a_d(x-1)^2 + x}, & x > 1, \end{cases} \tag{2}$$

where $y = f/f_c$; $x = \varepsilon/\varepsilon_c$; $a_a = 2.4–0.0125f_c$; $a_d = 0.157f_c 0.785–0.905$; $a_a$ and $a_d$ are the parameter values of the ascending and descending stages of the compressive stress-strain curve, respectively; $f_c$ is the peak compressive strength; $\varepsilon_c$ is the compressive strain corresponding to the peak compressive strength and taken as follows:

$$\varepsilon_c = \left(700 + 172\sqrt{f_c}\right) \times 10^{-6}. \tag{3}$$

*4.4.2. Tensile Behavior*

$$y = \begin{cases} 1.2x - 0.2x^6, & x \le 1, \\ \dfrac{x}{a_t(x-1)^{1.7} + x}, & x > 1, \end{cases} \tag{4}$$

where $y = f/f_t$; $x = \varepsilon/\varepsilon_t$; $a_t$ is the parameter values of descending stages of the tensile stress-strain curve; $f_t$ is the peak tensile strength; $\varepsilon_t$ is the tensile strain corresponding to the peak tensile strength and calculated as follows:

$$\varepsilon_t = f_t^{0.54} \times 65 \times 10^{-6}. \tag{5}$$

*4.5. Constitutive Models of Concrete Hollow Block.* The concrete block compressive and tensile stress-strain relationships adopted the models proposed by Jing [37] and Zheng [38], respectively, which could reasonably reflect the mechanical properties of the blocks during cyclic loading.

*4.5.1. Compressive Behavior*

$$y = \begin{cases} 1.53 - 0.53x^2, & x \le 1, \\ \dfrac{x}{\alpha(x-1)^2 + x}, & x > 1, \end{cases} \tag{6}$$

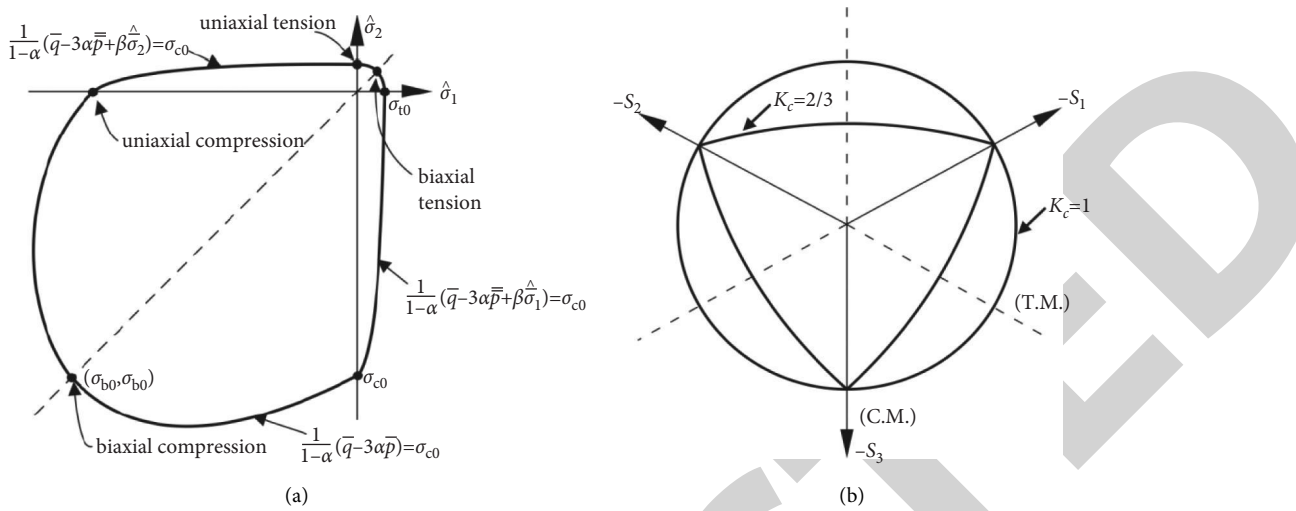


Figure 6: The yield surfaces and deviatoric plane of the CDP model [33].(a)Yield surfaces. (b) Deviatoric plane.

where $y = \sigma/f_u$; $x = \varepsilon/\varepsilon_c$; $\alpha$ is the parameter values of descending stages of the uniaxial compressive stress-strain curve, and taken as 5.0; $f_u$ is the uniaxial compressive strength of the blocks and computed by equation (7); $\varepsilon_c$ is the compressive strain corresponding to the uniaxial compressive strength and calculated by the equation .

$$f_u = k_1 f_1^{\beta}(1 + 0.07 f_2)k_2. \tag{7}$$

$$\varepsilon_c = 1192 + 70\sqrt{f_u}, \tag{8}$$

where $k_1$, $k_2$, and $\beta$ are taken as 0.46, 1.0, and 0.9 according to GB 50003–2011 [39]. $F_1$ and $f_2$ are the compressive strength of block and mortar, respectively.

*4.5.2. Tensile Behavior*

$$y = \begin{cases} x, & x \le 1, \\ \dfrac{x}{2(x-1)^{1.7} + x}, & x > 1, \end{cases} \tag{9}$$

where $y = \sigma/f_{tm}$; $x = \varepsilon/\varepsilon_{tm}$; $\varepsilon_{tm} = f_{tm}/E$; $f_{tm}$ is the tensile strength of blocks; $\varepsilon_{tm}$ is the tensile strain corresponding to the tensile strength; $E$ is the elasticity modulus of blocks, which is defined as follows

$$E = \frac{f_u}{8.66 + 0.51\sqrt{f_u}}. \tag{10}$$

*4.6. Damage Development.* Figure 7 shows the damage parameter in the CDP model, where the cracking strain and crushing strain (inelastic) are calculated as follows:

$$\begin{aligned} \tilde{\varepsilon}_t^{ck} &= \varepsilon_t - \frac{\sigma_t}{E_0}, \\ \tilde{\varepsilon}_c^{in} &= \varepsilon_c - \frac{\sigma_c}{E_0}. \end{aligned} \tag{11}$$

The plastic strain in tension and compression are written as follows:

$$\begin{aligned} \tilde{\varepsilon}_t^{pl} &= \tilde{\varepsilon}_t^{ck} - \frac{d_t}{(1-d_t)}\frac{\sigma_t}{E_c}, \\ \tilde{\varepsilon}_c^{pl} &= \tilde{\varepsilon}_c^{ck} - \frac{d_c}{(1-d_c)}\frac{\sigma_c}{E_c}. \end{aligned} \tag{12}$$

where $d_c$ and $d_t$ are the tensile and compressive damage parameters, respectively.

The damage parameter is defined as follows:

$$d_i = 1 - \sqrt{\frac{1-\sigma_i}{(E_0\varepsilon_i)}}, \tag{13}$$

where $E_0$ is the initial elastic modulus.

*4.7. Modelling of Steel Bars.* Considering the progressive damage and strength degradation under cycle loads, the constitutive model of the steel bar is depicted in Figure 8, where $\tilde{\varepsilon}_0^{pl}$ was the plastic strain corresponding to the damage initiation point, while $\tilde{\varepsilon}_f^{pl}$ was defined as a value that almost equals to zero, such as 0.00001 [40], by which the strength and stiffness degradation behavior up to failure could be simulated.

## 5. Finite Element Results and Analysis

*5.1. Model Validation.* The established finite element model is shown in Figure 9. The finite element results are compared with the test results as shown in Figure 10. The skeleton curves of a simulate specimen and test specimen almost coincide, which proves the reliability of the finite element model. The peak loads of the simulation and test are 159.8 kN and 154.1 kN, respectively; the peak load error is less than 3%. The difference in the shape of the curves may be owing to the that the bottom beam was not sufficiently restricted in the test. In total, the finite element model can be further used in the subsequent simulations.

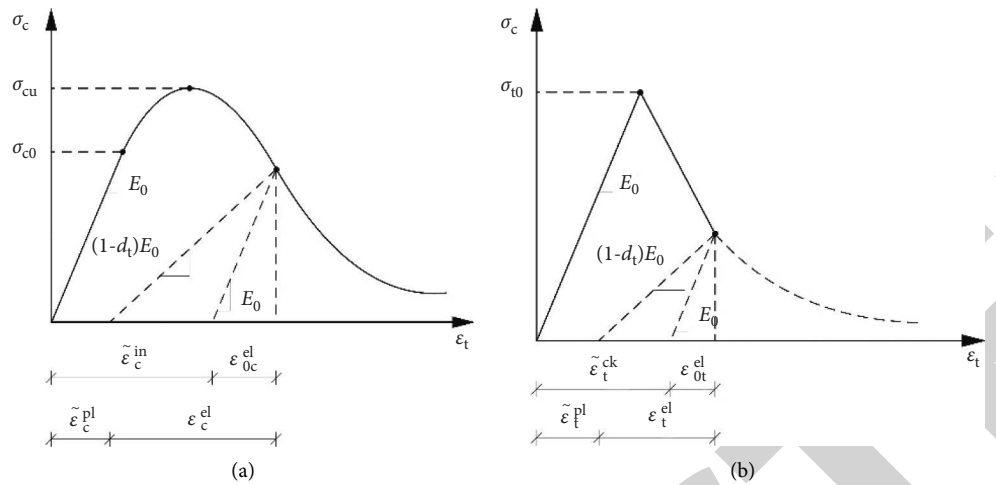


Figure 7: Damage development in compression and tension. (a) Compression damage. (b) Tension damage.

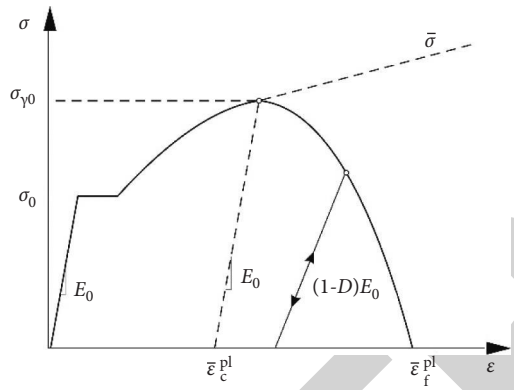


Figure 8: Stress-strain curve with progressive damage.

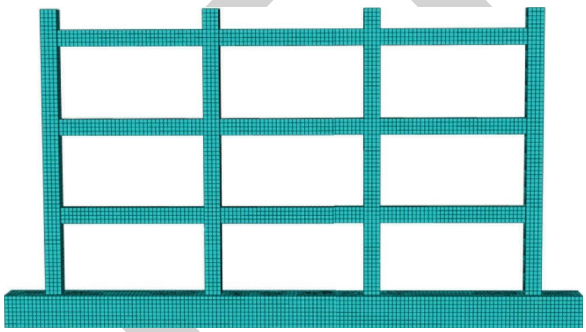

Figure 9: The established finite element model.

*5.2. Hysteretic Curve.* The hysteretic curve of each specimen is shown in Figure 11. They are compared in Figure 12 to investigate the effect of each parameter. From Figures 11 and 12, it can be seen that the hysteretic curves of all specimens exhibit similar shapes. This indicates that the opening rates, the position of infill walls, and the block strength did not change the shape of the hysteretic curves. It can be seen from Figures 11(b)–11(e) that the ultimate bearing capacity of the specimen decreases with the increase of the opening rate of the filled wall, and the fullness of the hysteretic curves decreases with the enlargement of opening rates of infill walls. Therefore, the openings in the infilled walls can enhance the stiffness of frames but weaken the energy consumption capacity of the specimens under earthquake load. Moreover, Figures 12(f)–12(i) show that the fullness of specimens under different block strengths almost kept the same. This indicates that the block strength has little effect on the seismic behavior of specimens.

*5.3. Skeleton Curves.* Figure 13 illustrates the skeleton curves extracted from the maximum trajectory from the hysteretic curves under each level of the displacement cycle. The load and displacement of the main characteristic points of each specimen are shown in Table 4. Figures 13(a) and 13(b) show that the bearing capacity of all specimens reduces sequentially with the increasing opening ratio. They also decreased after removing the infill walls on the first floor. The peak load of KJ-1 was 154.1 kN. The peak loads of KJ-T-1-KJ-T-4 were 870.5 kN, 594.7 kN, 489.7 kN, and 363.2 kN, respectively. Compared with KJ-1, the peak bearing capacity of specimens with infill walls could increase by about 4.5 times with infill walls; this indicates that ignoring the effect of infill walls could significantly underestimate the seismic behavior of frames. The peak bearing capacity is not decreased linearly with an increasing opening rate. The effect of the initial opening rate on seismic behavior is the maximum. The peak bearing capacities of KJ-T-5 and KJ-T-6 were 569.7 kN, and 317.5 kN, respectively. The curves of KJ-1, KJ-T-3 and KJ-T-4 have a relatively slower descent part than those of the KJ-T-1 and KJ-T-2, which demonstrates the ductility of the specimens enhance with the increase of the opening area in the masonry walls. Figure 10(c) shows that the peak bearing capacity of KJ-T-7 and KJ-T-8 is 446.0 kN and 538.3 kN, respectively. This indicates that the bearing capacity of specimens could be improved by increasing the block strength.

*5.4. Energy Dissipation.* Figure 14 shows the sketch of the energy dissipation coefficient, which is calculated as follows:

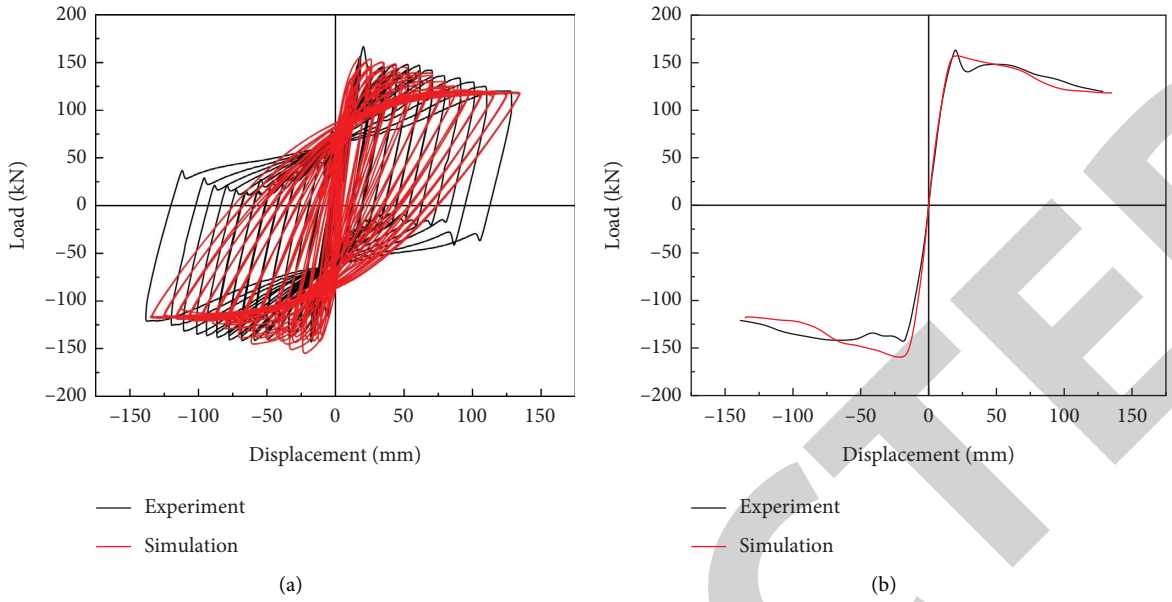


Figure 10: The comparison between experimental results and simulation results. (a) Hysteretic curves. (b) Skeleton curves.

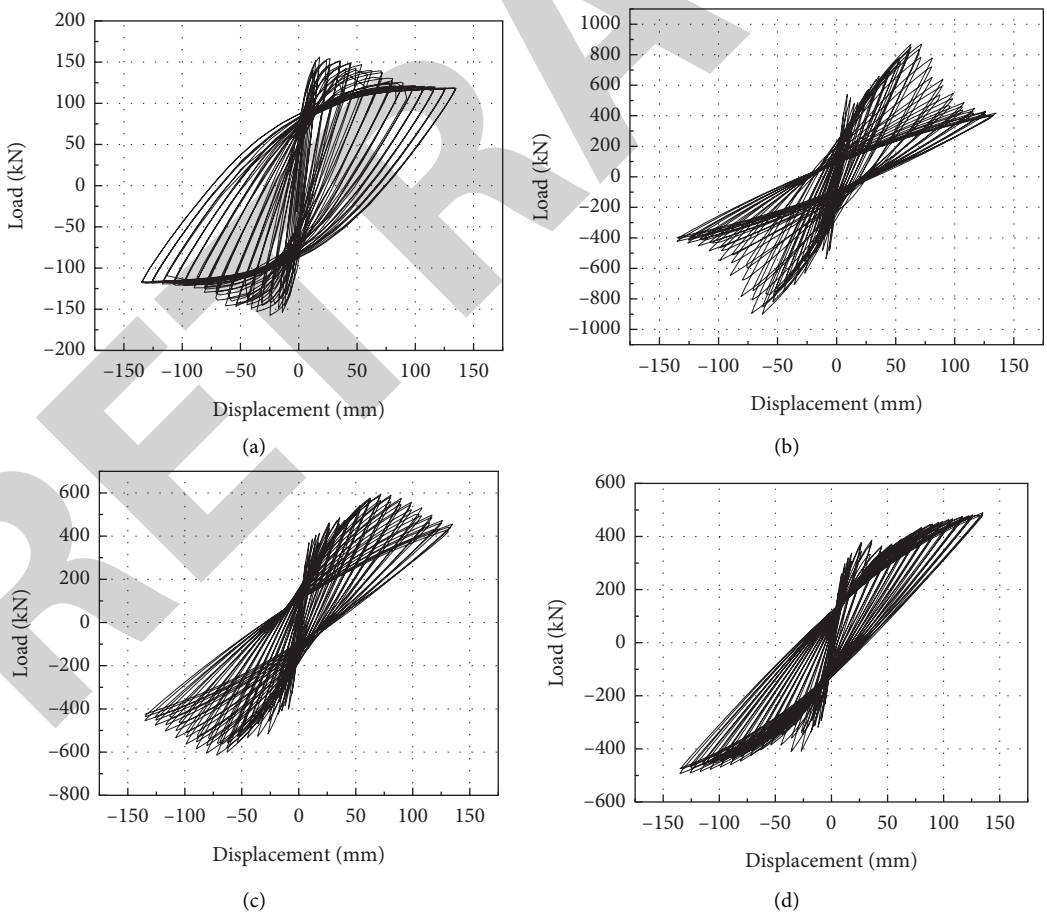

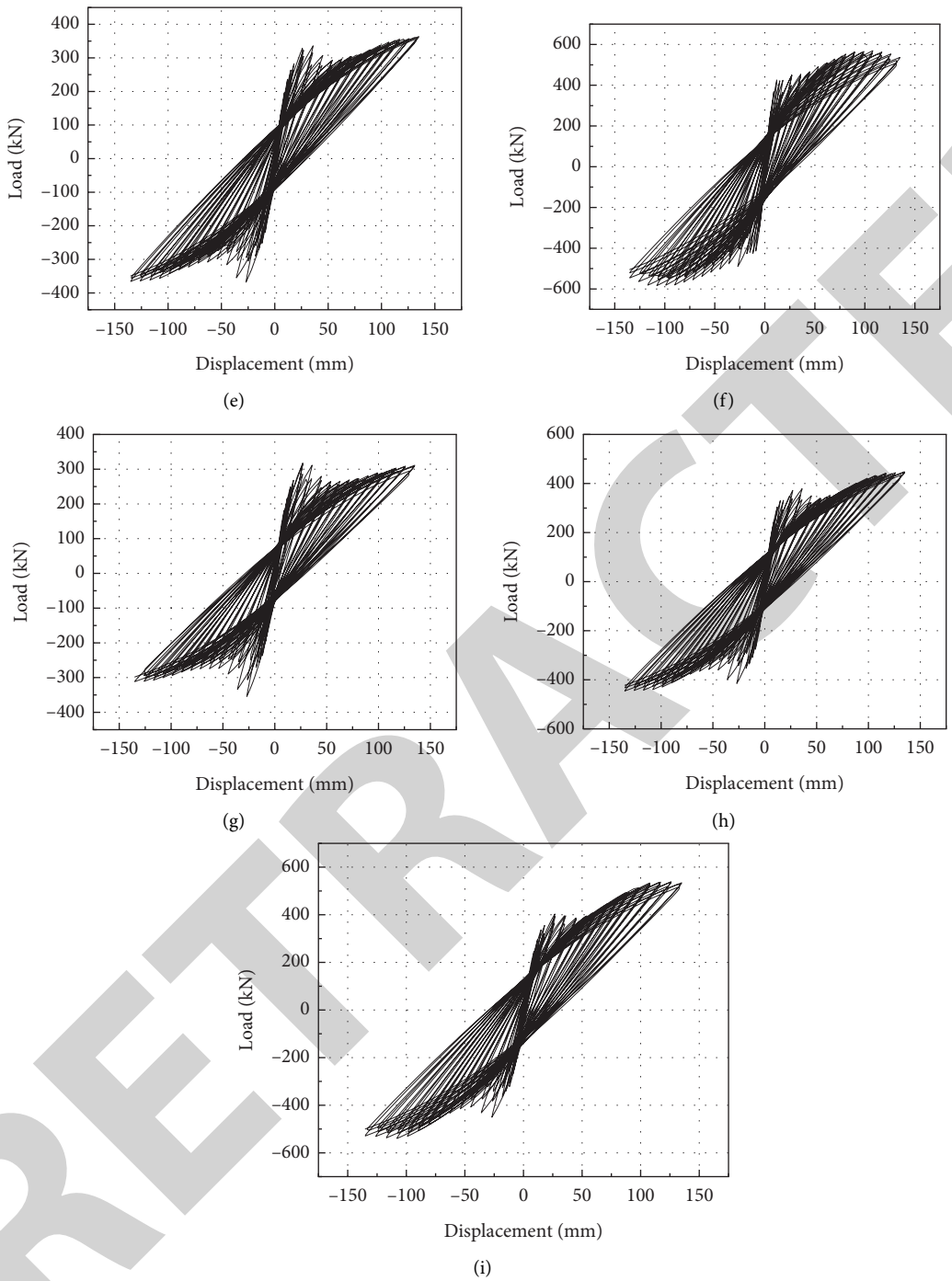


Figure 11: The hysteretic curve of each specimen. (a) KJ-1, (b) KJ-T-1, (c) KJ-T-2, (d) KJ-T-3, (e) KJ-T-4, (f) KJ-T-5, (g) KJ-T-6, (h) KJ-T-7, and (i) KJ-T-8.

$$E = \frac{1}{2\pi} \frac{S_{(ABC+CDA)}}{S_{(OBE+ODF)}}, \tag{14}$$

where $S_{(\mathrm{ABC}+\mathrm{CDA})}$ denotes the energy dissipation value of the specimen and $S_{(\mathrm{OBE}+\mathrm{ODF})}$ is the energy dissipation value by the equivalent elastic object at the same displacement.

The results are summarized in Table 5. The energy dissipation coefficient of KJ-1 is the biggest, although its bearing capacity is the smallest in the specimens built by FE. For the frames with masonry-infilled walls, the energy dissipation coefficients decline as the size of the openings increases, which indicates the negative effect of openings on energy dissipation of the frames with infilled walls. The

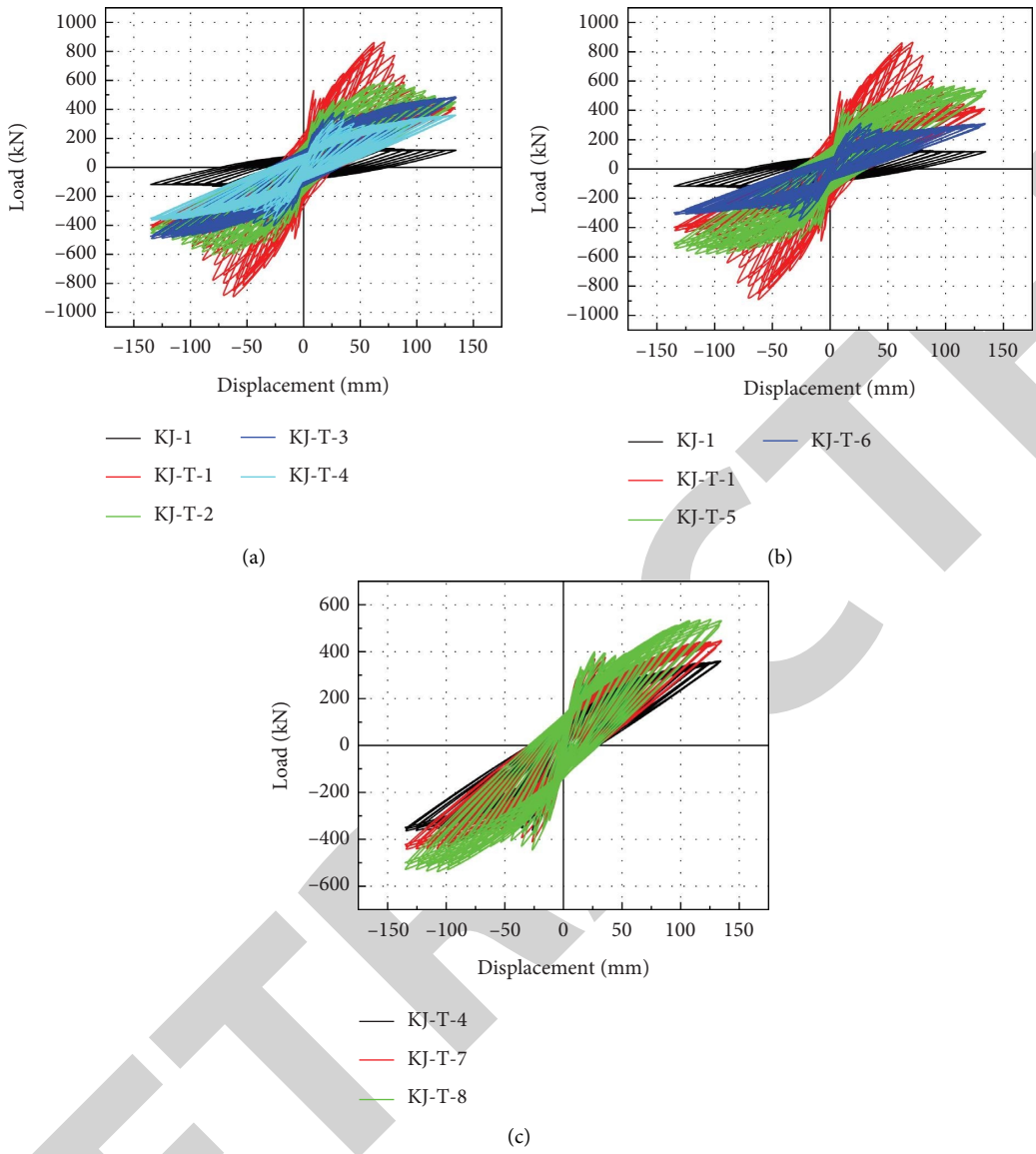


Figure 12: The effect of different parameters on hysteretic curve. (a) The effect of opening rate. (b) The effect of the infill falls position. (c) The effect of the block strength.

energy dissipation coefficients of specimens with different block strengths are very close. Therefore, the block strengths have little effect on the energy dissipation coefficient.

*5.5. Stiffness Degradation.* Stiffness degradation refers to the phenomenon that the stiffness of a structure decreases gradually, and the cumulative damage increases gradually under the action of cyclic load. The stiffness degradation of the specimens is represented by the secant stiffness, and the stiffness degradation curves based on the skeleton curves are presented in Figure 15. At the early stage of loading, cracks appear, and the damage to the specimen increases rapidly. After the specimen yields, the concrete protective layer gradually stops working, and the damage accumulation and stiffness degradation speed slow down. After the peak load, the specimen entered the plastic stage, and no new cracks were generated. The stiffness of the specimen tends to be stable. The initial stiffness of the specimens decreases successively with the increase of the opening size in the infilled walls. The initial stiffness of KJ-T-1 is about five times than that of KJ-1, which clears the importance of the masonry-infilled walls to the stiffness of the frame. The stiffness of all specimens degraded sharply at the initial loading phase, and the rate of stiffness degeneration became slow when the specimens yielded. The total reduced stiffness values were less

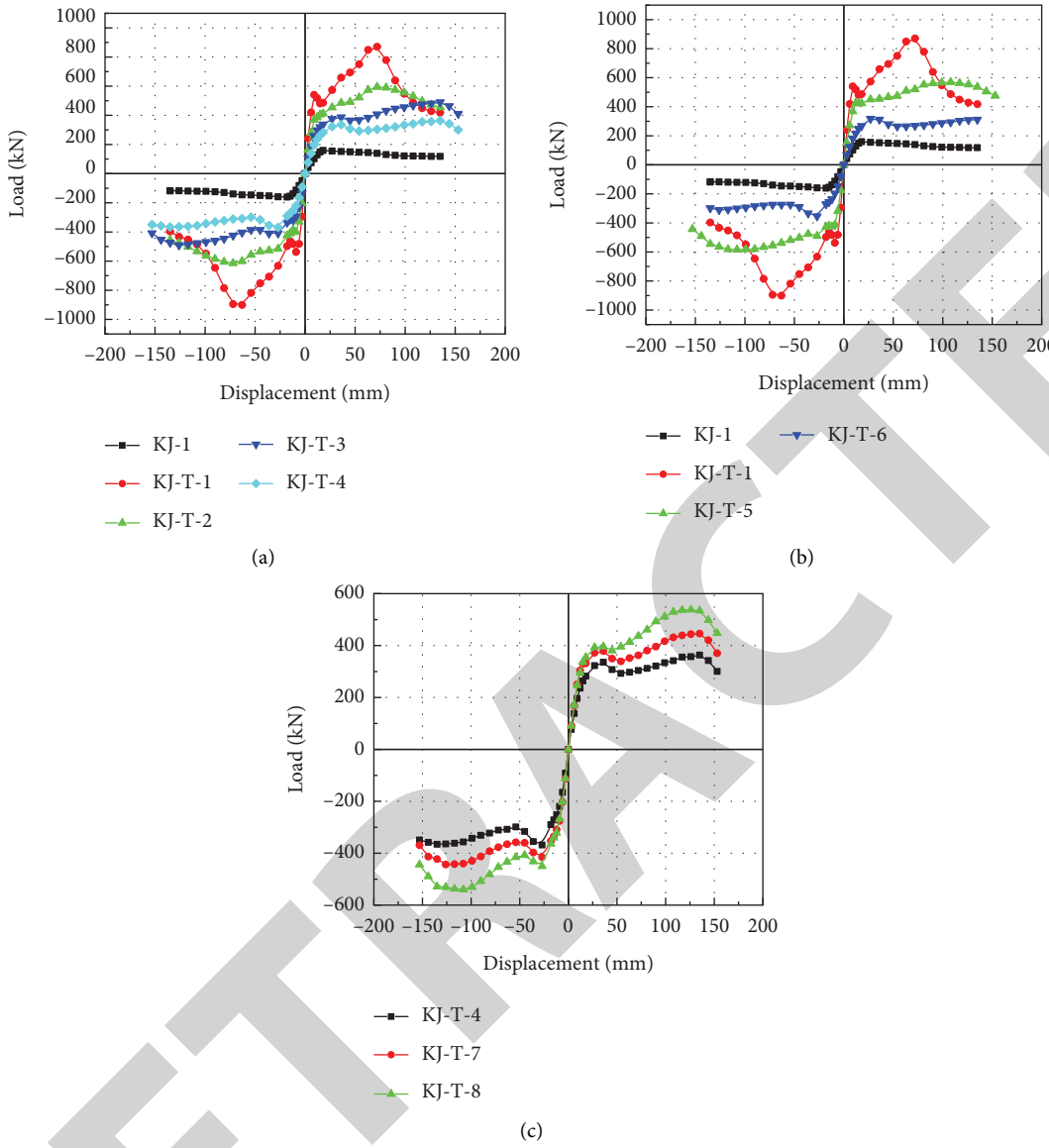


Figure 13: The effect of different parameters on skeleton curves. (a) The effect of opening rate. (b) The effect of the infill falls position. (c) The effect of the block strength.

than 30% of the initial stiffness before the yield point. The stiffness of specimens changes a little with different block strengths.

*5.6. Ductility.* The ductility of the specimens is measured by the displacement ductility coefficient, which can be calculated using the ultimate displacement divided by the yield displacement. The ultimate displacement refers to the displacement corresponding to the load dropping to the 85% bearing capacity of the specimens. Table 6 shows the displacement ductility coefficient of each specimen.

For specimens KJ-T-1 and -KJ-T-4, the ductility coefficient of the specimens increases as the opening rate increases and that of KJ-T-4 is the largest. It is clear that the opening in the infilled walls can improve the ductility of the frames. The effect of block strength on the ductility coefficient is irregular.

*5.7. Failure Characteristic.* Taking specimens, such as KJ-T-1, KJ-T-4, KJ-T-5, and KJ-T-8 as an example, the effects of openings, the position of infill walls, and the block strength on the failure characteristic were analyzed in this section. The failure modes of specimens are shown in Figure 16–19.

Figure 16 shows that the masonry-infilled walls make the stress distribution in the frame more uniform, and the stress of the steel bar is evenly distributed along the beams and columns without obvious concentration. Compared with a bare frame, the plastic hinge damage is decreased. The maximum plastic strain is found in the concrete connections

Table 4: The results of the energy dissipation coefficient.

| Specimen | Loading direction | *Yield point* | | *Peak point* | |
|---|---|---|---|---|---|
| | | Load/(kN) | Displacement/(mm) | Load/(kN) | Displacement/(mm) |
| KJ-1 | Push | 144.0 | 15.24 | 154.1 | 19.05 |
| | Pull | −131.6 | −15.11 | −143.0 | −18.87 |
| KJ-T-1 | Push | 482.2 | 15.74 | 870.5 | 72 |
| | Pull | −489.3 | −17.31 | −900.7 | −63 |
| KJ-T-2 | Push | 406.3 | 15.77 | 594.7 | 72 |
| | Pull | −414.0 | −15.67 | −614.3 | −72 |
| KJ-T-3 | Push | 346.3 | 20.25 | 489.7 | 135 |
| | Pull | −349.3 | −19.51 | −493.4 | −135 |
| KJ-T-4 | Push | 287.9 | 19.35 | 363.2 | 135 |
| | Pull | −300.0 | −19.23 | −368.2 | −27 |
| KJ-T-5 | Push | 421.9 | 14.93 | 569.7 | 108 |
| | Pull | −420.0 | −15.00 | −583.7 | −108 |
| KJ-T-6 | Push | 271.0 | 18.55 | 317.5 | 27 |
| | Pull | −290.1 | −20.07 | −354.3 | −27 |
| KJ-T-7 | Push | 334.1 | 18.51 | 446.0 | 135 |
| | Pull | −353.5 | −18.21 | −445.3 | −135 |
| KJ-T-8 | Push | 383.4 | 24.69 | 538.3 | 126 |
| | Pull | −431.8 | −24.97 | −539.7 | −108 |

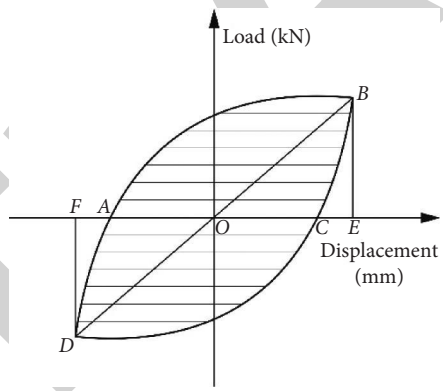


Figure 14: Sketch of the energy dissipation coefficient.

Table 5: The results of the energy dissipation coefficient.

| Specimen | *Accumulated energy dissipation/(kN·m)* | | *The energy dissipation coefficient* | |
|---|---|---|---|---|
| | Yield point | Peak point | Yield point | Peak point |
| KJ-1 | 2.34 | 183.34 | 0.1606 | 0.2032 |
| KJ-T-1 | 9.01 | 352.43 | 0.0685 | 0.1148 |
| KJ-T-2 | 6.41 | 364.15 | 0.0671 | 0.1133 |
| KJ-T-3 | 8.95 | 249.67 | 0.0535 | 0.1047 |
| KJ-T-4 | 4.01 | 319.39 | 0.0457 | 0.1027 |
| KJ-T-5 | 5.60 | 618.15 | 0.0554 | 0.1079 |
| KJ-T-6 | 3.65 | 459.05 | 0.0440 | 0.0686 |
| KJ-T-7 | 6.04 | 604.66 | 0.0559 | 0.1020 |
| KJ-T-8 | 14.43 | 499.47 | 0.0729 | 0.1032 |

between the infilled walls and the columns, and gradually decreases in the horizontal direction of the walls. The concrete at the beams end, columns top, and columns foot emerges obvious plastic strain.

From Figures 16 and 17, it can be seen the stress of the steel bar and concrete gradually transfers to the core area of the joints and the column foot. The plastic strain in the hole corner of the infilled walls is the largest and decreases in turn

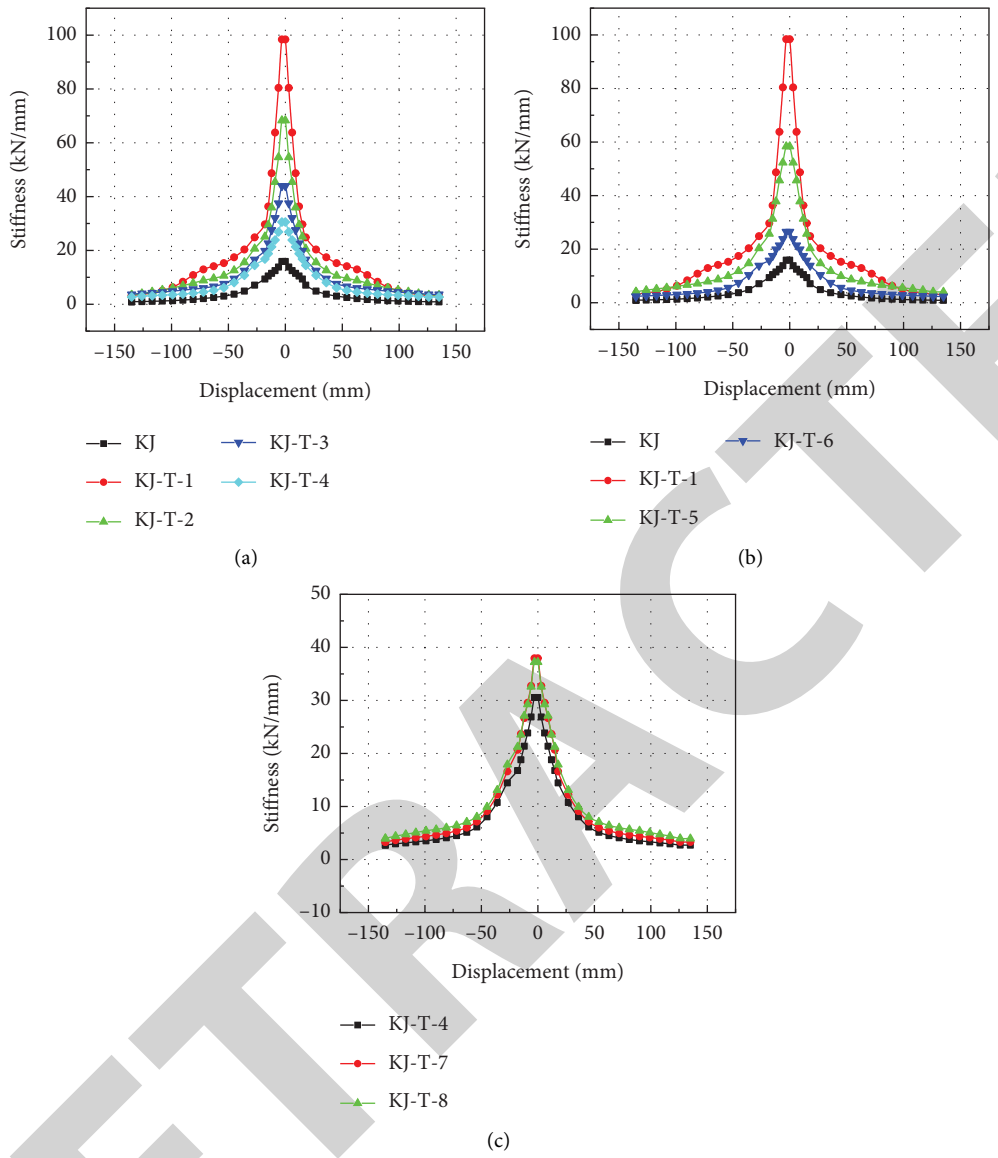


Figure 15: Stiffness degradation. (a) The effect of opening rate. (b) The effect of the infill falls position. (c) The effect of the block strength.

Table 6: Displacement ductility coefficient.

| Specimen number | *Loading direction* | | Mean |
|---|---|---|---|
| | Positive | Negative | |
| KJ-1 | 5.278 | 5.547 | 5.413 |
| KJ-T-1 | 5.278 | 5.547 | 5.412 |
| KJ-T-2 | 5.771 | 5.536 | 5.654 |
| KJ-T-3 | 7.176 | 6.925 | 7.050 |
| KJ-T-4 | 9.279 | 9.408 | 9.343 |
| KJ-T-5 | 5.882 | 6.023 | 5.953 |
| KJ-T-6 | 6.084 | 5.918 | 6.001 |
| KJ-T-7 | 5.632 | 5.484 | 5.558 |
| KJ-T-8 | 6.991 | 7.711 | 7.351 |

with the increase of the opening size. The effect of the infilled walls to distribute stress declines in sequence and the failure mechanism of the "beam hinge" is gradually severe.

Figure 18 shows that the stress concentration occurred at the column foot; this indicates that specimen KJ-T-5 failed with a column hinge damage. This is caused by lower stiffness in the first floor than others, which resulting in absorbing much more energy in the first floor.

Figure 19 shows that increasing the block strength could make the stress distribution more uniform.

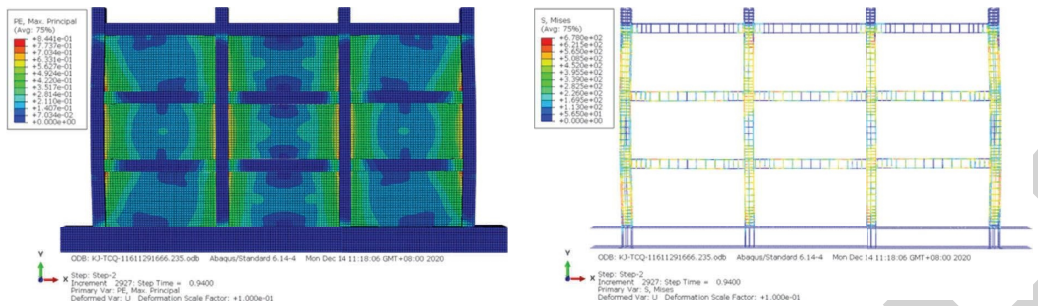

(a) (b)

Figure 16: Specimen KJ-T-1. (a) Concrete plastic strain contour. (b) Steel bar stress contour.

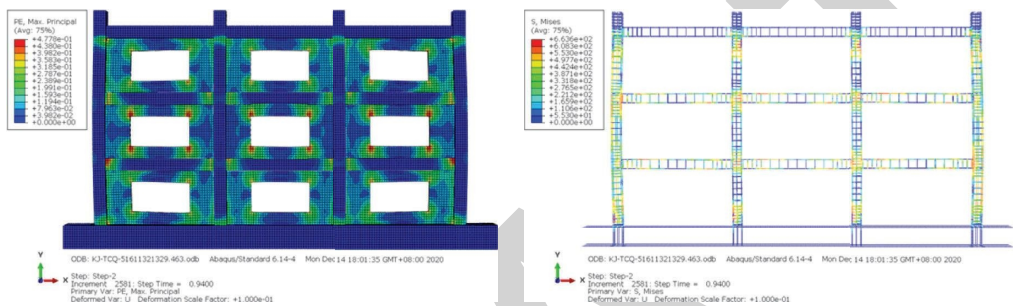

(a) (b)

Figure 17: Specimen KJ-T-4. (a) Concrete plastic strain contour. (b) Steel bar stress contour.

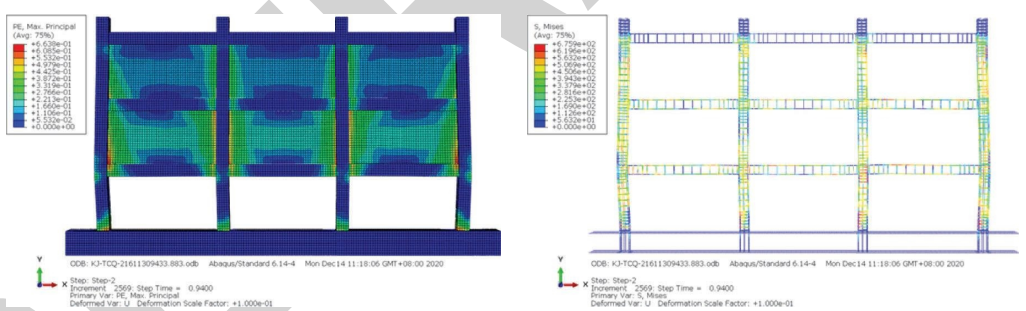

(a) (b)

Figure 18: Specimen KJ-T-5. (a) Concrete plastic strain contour. (b) Steel bar stress contour.

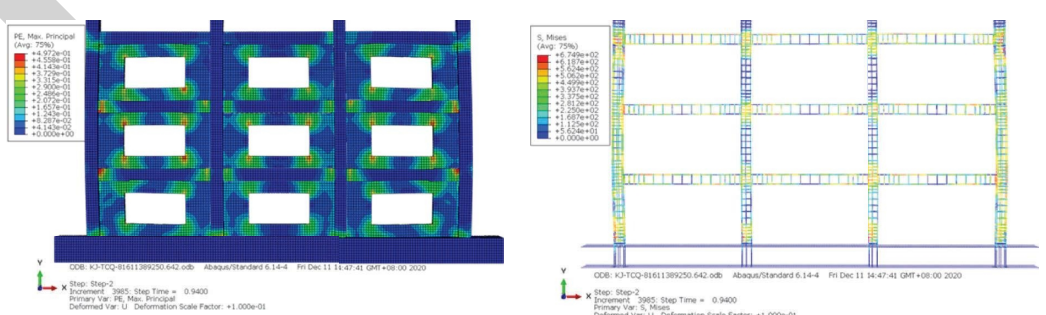

(a) (b)

Figure 19: Specimen KJ-T-8. (a) Concrete plastic strain contour. (b) Steel bar stress contour.

## 6. Conclusions

In this paper, the seismic performance of the frame was studied using pseudostatic testing, and the seismic performance of RC frames with different openings, locations, and block strengths of masonry-infilled walls was studied by finite element analysis. Based on the results, the following conclusion can be drawn.

(1) When the test frame failed, the steel bars in the beam end yielded or ruptured, and the interstory displacement angle exceeded the limits specified in the code GB 50011–2010 and ASCE 7–05. The hysteretic curve was a "bow" shape, which indicated good energy dissipation of the specimen.

(2) The skeleton curves of the tested specimen and finite element model were relatively close. Still, the hysteresis curve shape was slightly different, which may be caused by the bottom beam of the test specimen not being sufficiently restricted. The established FE model was in good agreement with the test specimen.

(3) The infilled walls could improve the frame's bearing capacity, stiffness, and ductility while reducing energy dissipation capacity. All seismic performance indexes were gradually decreased with the opening size enlarged except ductility. The block strength has little effect on the stiffness degradation and energy dissipation capacity but could improve the bearing capacity.

(4) The masonry-infilled walls without openings distributed the frame stress more uniformly, and no stress concentration occurred in the beams and columns. As the size of the openings increases, opposite to the stress change at the corner of the openings, the stress concentration phenomenon in the core area of the joints and the columns foot becomes gradually serious. Removing the infill walls on the first floor would make the frame fail with column hinge damage. Increasing the block strength could make the stress distribution more uniform.

## Data Availability

No data were used to support this study.

## Conflicts of Interest

The authors declare there are no conflicts of interest regarding the publication of this paper.

## Acknowledgments

The findings and opinions expressed in this paper are those of the authors and do not necessarily reflect those of the sponsors. The authors gratefully acknowledge the financial support provided by the National Natural Science Foundation of China (51578077).

## References

[1] H. Varum, A. Furtado, H. Rodrigues, J. Dias-Oliveira, N. Vila-Pouca, and A. Arede, "Seismic performance of the infill masonry walls and ambient vibration tests after the Ghorka 2015, Nepal earthquake," *Bulletin of Earthquake Engineering*, vol. 15, no. 3, pp. 1185–1212, 2017.

[2] X. Zhou, X. Kou, Q. Peng, and J. Cui, "Influence of infill wall configuration on failure modes of RC frames," *Shock and Vibration*, vol. 2018, Article ID 6582817, 14 pages, 2018.

[3] A. D. Dautaj, Q. Kadiri, and N. Kabashi, "Experimental study on the contribution of masonry infill in the behavior of RC frame under seismic loading," *Engineering Structures*, vol. 165, no. 15, pp. 27–37, 2018.

[4] C. V. R. Murty and S. K. Jain, "Beneficial Influence of Masonry Infill walls on Seismic Performance of RC Frame Buildings," in *Proceedings of the 12th World Conference on Earthquake Engineering*, Auckland, New Zealand, 2000.

[5] A. Fiore, A. Netti, and P. Monaco, "The influence of masonry infill on the seismic behaviour of RC frame buildings," *Engineering Structures*, vol. 44, pp. 133–145, 2012.

[6] S. Sattar and A. B. Liel, "Seismic Performance of Reinforced concrete Frame Structures with and without Masonry Infill walls," in *Proceedings of the 9th US National and 10th Canadian conference on earthquake engineering*, Toronto, Canada, 2010.

[7] P. G. Asteris, D. M. Cotsovos, C. Z. Chrysostomou, A. Mohebkhah, and G. Al-Chaar, "Mathematical micromodeling of infilled frames: state of the art," *Engineering Structures*, vol. 56, pp. 1905–1921, 2013.

[8] M. Dolšek and P. Fajfar, "The effect of masonry infills on the seismic response of a four-storey reinforced concrete frame—a deterministic assessment," *Engineering Structures*, vol. 30, no. 7, pp. 1991–2001, 2008.

[9] B. Pantò, I. Calio, and P. B. Lourenço, "Seismic safety evaluation of reinforced concrete masonry infilled frames using macro modelling approach," *Bulletin of Earthquake Engineering*, vol. 15, no. 9, pp. 3871–3895, 2017.

[10] A. Mansouri, M. S. Marefat, and M. khanmohammadi, "Experimental evaluation of seismic performance of low-shear strength masonry infills with openings in reinforced concrete frames with deficient seismic details," *The Structural Design of Tall and Special Buildings*, vol. 23, no. 15, pp. 1190–1210, 2014.

[11] X. Wang, W. Zhao, J. Kong, and T. Zhao, "Numerical investigation on the influence of in-plane damage on the out-of-plane behavior of masonry infill walls," *Advances in Civil Engineering*, vol. 2020, no. 2, Article ID 6276803, 16 pages, 2020.

[12] L. Wang, K. Qian, F. Fu, and X. F. Deng, "Experimental study on the seismic behaviour of reinforced concrete frames with different infill masonry," *Magazine of Concrete Research*, vol. 72, no. 23, pp. 1203–1221, 2020.

[13] D. Penava, V. Sarhosis, I. Kožar, and I. Guljas, "Contribution of RC columns and masonry wall to the shear resistance of masonry infilled RC frames containing different in size window and door openings," *Engineering Structures*, vol. 172, pp. 105–130, 2018.

[14] J. Zovkic, V. Sigmund, and I. Guljas, "Cyclic testing of a single bay reinforced concrete frames with various types of masonry infill," *Earthquake Engineering & Structural Dynamics*, vol. 42, no. 8, pp. 1131–1149, 2013.

[15] Y. Zhang, P. Yang, and Z. Zhou, "Seismic performance analysis of recycled masonry infill wall-shaped steel recycled

concrete frame structure," *Building Structure*, vol. 52, no. 13, pp. 62–68, 2022.

[16] S. H. Basha and H. B. Kaushik, "Behavior and failure mechanisms of masonry-infilled RC frames (in low-rise buildings) subject to lateral loading," *Engineering Structures*, vol. 111, pp. 233–245, 2016.

[17] I. A. M. Budiwati and M. Sukrawa, "Development of diagonal strut width formula for infill wall with reinforced opening in modeling seismic behavior of RC infilled frame structures," *Conference proceedings*, vol. 1977, no. 1, Article ID 20062, 2018.

[18] P. B. Shing and A. B. Mehrabi, "Behaviour and analysis of masonry-infilled frames," *Progress in Structural Engineering and Materials*, vol. 4, no. 3, pp. 320–331, 2002.

[19] H. Jin, X. Jin, and J. Dai, "Analysis on failure modes and numerical simulations of masonry-infilled reinforced concrete frame structures," *China Civil Engineering Journal*, vol. 47, no. S2, pp. 175–180, 2014.

[20] A. F. Mohammad, K. Fatima, and A. K. Rashid, "Finite element micro-modelling of RC frames with variant configurations of infill masonry," *Structural Engineering & Mechanics*, vol. 81, no. 4, pp. 395–409, 2022.

[21] K. M. Dolatshahi and M. Yekrangnia, "Out of plane strength reduction of unreinforced masonry walls because of in-plane damages," *Earthquake Engineering & Structural Dynamics*, vol. 44, no. 13, pp. 2157–2176, 2015.

[22] D. V. Mallick and R. T. Severn, "The behaviour of infilled frames under static loading," *Proceedings - Institution of Civil Engineers*, vol. 38, no. 4, pp. 639–656, 1967.

[23] D. V. Mallick and R. P. Garg, "Effect of openings on the lateral stiffness of infilled frames," *Proceedings - Institution of Civil Engineers*, vol. 49, no. 2, pp. 193–209, 1971.

[24] Liauw, T. E. Chang, and K. Kwok-Hung, "Nonlinear behaviour of non-integral infilled frames," *Computers & Structures*, vol. 18, no. 3, pp. 551–560, 1984.

[25] P. G. Asteris, "Lateral stiffness of brick masonry infilled plane frames," *Journal of Structural Engineering*, vol. 129, no. 8, pp. 1071–1079, 2003.

[26] P. G. Asteris, "Finite element micro-modeling of infilled frames," *Electronic Journal of Structural Engineering*, vol. 8, no. 8, pp. 1–11, 2008.

[27] H. R. Lotfi and P. B. Shing, "An appraisal of smeared crack models for masonry shear wall analysis," *Computers & Structures*, vol. 41, no. 3, pp. 413–425, 1991.

[28] I. Koutromanos, A. Stavridis, P. B. Shing, and K. Willam, "Numerical modeling of masonry-infilled RC frames subjected to seismic loads," *Computers & Structures*, vol. 89, no. 11-12, pp. 1026–1037, 2011.

[29] I. Koutromanos, *Numerical Analysis of Masonry-Infilled Reinforced concrete Frames Subjected to Seismic Loads and Experimental Evaluation of Retrofit Techniques*, University of California, San Diego, 2011.

[30] P. B. Lourenço and J. G. Rots, "Multisurface interface model for analysis of masonry structures," *Journal of Engineering Mechanics*, vol. 123, no. 7, pp. 660–668, 1997.

[31] GB 50011-2010, *Code for Seismic Design of Buildings*, China Architecture and Building Press, Beijing, China, 2016.

[32] ASCE/SEI 7-10, *Minimum Design Loads for Buildings and Other Structures*, American Society of Civil Engineer (ASCE), USA, 2010.

[33] S. Dassault, *ABAQUS 6.14 Analysis User's Guide," Materials*, USA, 2014.

[34] J. Lubliner, J. Oliver, S. Oller, and E. Onate, "A plastic-damage model for concrete," *International Journal of Solids and Structures*, vol. 25, no. 3, pp. 299–326, 1989.

[35] J. Lee and G. L. Fenves, "Plastic-damage model for cyclic loading of concrete structures," *Journal of Engineering Mechanics*, vol. 124, no. 8, pp. 892–900, 1998.

[36] G B 50010-2010, *Code for Design of concrete Structures*, China Planning Press, Beijing, China, 2015.

[37] Y. C. Jing, *Experimental Study on Uniaxial Compressive Property and Stress-Stain Relationship of Hollow concrete 190 Block Masonry*, Harbin Institute of Technology, Harbin, China, 2012.

[38] N. N. Zheng, *Research on Seismic Behavior of Masonry Structures with Fabricated Tie-Columns*, Chongqing University, Chongqing, China, 2010.

[39] G B 50003-2011, *Code for Design of Masonry Structures*, China Architecture and Building Press, Beijing, China, 2011.

[40] Y. Sun, Y. Liu, T. Wu, X. Liu, and H. Lu, "Numerical analysis on flexural behavior of steel fiber-reinforced LWAC beams reinforced with GFRP bars," *Applied Sciences*, vol. 9, no. 23, p. 5128, 2019.